



LAWRENCE  
LIVERMORE  
NATIONAL  
LABORATORY

# Kinetically Controlled Three-Dimensional Complex of Reticular Metal–Elastomer Nanophases

S. Chae, W. Choi, L. J. Nebel, C. H. Cho, Q. A. Besford, A. Knapp, P. Makushko, Y. Zabala, O. Pylypovskiy, M. W. Jeong, S. Avdoshenko, O. Sander, D. Makarov, A. Fery, J. Y. Oh, T. I. Lee

March 6, 2023

Nature Communications

## **Disclaimer**

---

This document was prepared as an account of work sponsored by an agency of the United States government. Neither the United States government nor Lawrence Livermore National Security, LLC, nor any of their employees makes any warranty, expressed or implied, or assumes any legal liability or responsibility for the accuracy, completeness, or usefulness of any information, apparatus, product, or process disclosed, or represents that its use would not infringe privately owned rights. Reference herein to any specific commercial product, process, or service by trade name, trademark, manufacturer, or otherwise does not necessarily constitute or imply its endorsement, recommendation, or favoring by the United States government or Lawrence Livermore National Security, LLC. The views and opinions of authors expressed herein do not necessarily state or reflect those of the United States government or Lawrence Livermore National Security, LLC, and shall not be used for advertising or product endorsement purposes.

# **Kinetically Controlled Gold-Silicone Elastomer Nanophases for Environmentally Resilient Stretchable Electronics**

*Soosang Chae<sup>1</sup>†, Won Jin Choi<sup>2</sup>†\*, Lisa Julia Nebel<sup>3</sup>, Chang Hee Cho<sup>4</sup>, Quinn A. Besford<sup>1</sup>, André Knapp<sup>1</sup>, Pavlo Makushko<sup>5</sup>, Yevhen Zabala<sup>5,6</sup>, Oleksandr Pylypovskyi<sup>5,7</sup>, Min Woo Jeong<sup>8</sup>, Stanislav Avdoshenko<sup>9</sup>, Oliver Sander<sup>3</sup>, Denys Makarov<sup>5</sup>, Yoon Jang Chung<sup>10</sup>, Andreas Fery<sup>1,11</sup>, Jin Young Oh<sup>8\*</sup> and Tae Il Lee<sup>4\*</sup>*

<sup>1</sup>IPF - Leibniz-Institut für Polymerforschung Dresden e.V., Institute of Physical Chemistry and Polymer Physics, 01069 Dresden, Germany.

<sup>2</sup>Lawrence Livermore National Laboratory, 7000 East Ave., Livermore, California 94550, USA

<sup>3</sup>Institut für Numerische Mathematik, Technische Universität Dresden, Zellescher Weg 12–14, 01069 Dresden, Germany.

<sup>4</sup>Department of Materials Science and Engineering, Gachon University, Seong-nam, Gyeonggi 13120, Republic of Korea.

<sup>5</sup>Helmholtz-Zentrum Dresden-Rossendorf e.V., Institute of Ion Beam Physics and Materials Research, 01328 Dresden, Germany.

<sup>6</sup>The H. Niewodniczanski Institute of Nuclear Physics, Polish Academy of Sciences, 31-348 Krakow, Poland.

<sup>7</sup>Kyiv Academic University, 03142 Kyiv, Ukraine

<sup>8</sup>Department of Chemical Engineering (Integrated Engineering Program), Kyung Hee University, Yongin 17104, Republic of Korea.

<sup>9</sup>IFW - Leibniz-Institut für Festkörper- und Werkstoffforschung e.V., Institute for Solid State Research, 01069 Dresden, Germany.

<sup>10</sup>Department of Chemical and Biological Engineering, Korea University, Seoul, 02841 Republic of Korea.

<sup>11</sup>Chair for Physical Chemistry of Polymeric Materials Technische Universität Dresden, Mommsenstr. 4, 01062 Dresden, Germany.

†These authors contributed equally to this work

\*Corresponding Authors

## 1 **Abstract**

2 **Nanophase mixtures, leveraging the complementary strengths of each component, are**  
3 **vital for composites to overcome limitations posed by single elemental materials. Among**  
4 **these, metal-elastomer nanophases are particularly important, holding various practical**  
5 **applications for stretchable electronics. However, the methodology and understanding of**  
6 **nanophase mixing metals and elastomers are extremely limited due to difficulties in**  
7 **blending caused by thermodynamic incompatibility. Here, we present a controlled**  
8 **method using kinetics to mix Au atoms with dimethylsiloxane chains on the nanoscale. We**  
9 **found that the chain migration flux and metal deposition rate are key factors, allowing**  
10 **the formation of reticular nanophases when kinetically in-phase. Moreover, we observed**  
11 **spontaneous structural evolution, resulting in gyrified structures akin to the human brain.**  
12 **The hybridized gyrified reticular nanophases exhibit strain-invariant metallic electrical**  
13 **conductivity up to 156% areal strain, unparalleled durability in organic solvents and**  
14 **aqueous environments with pH 2–13, and remarkable mechanical robustness, ideal for**  
15 **environmentally resilient devices.**

## 16 **Main**

17 Nanophase mixtures serve as crucial building blocks for functional composites because  
18 they can potentially maximize synergistic effects by leveraging the strengths of each component  
19 without any compromise<sup>1–4</sup>. However, when combining materials that lack strong mutual  
20 interaction, thermodynamically driven phase separation hinders the blending of their chemical  
21 and physical properties<sup>5–8</sup>. This challenge is particularly pronounced in composites of metals  
22 and elastomers for stretchable conducting membranes<sup>8–11</sup>. Such membranes have long sought  
23 after properties that include metal-like conductivity, rubber-like elasticity, mechanical  
24 durability, and physicochemical resilience<sup>12–15</sup>. Nevertheless, creating conductive metal-  
25 elastomer nanophase mixtures is challenging, as the simple physical mixing of metal

1 nanoparticles (or nanowires)<sup>12,13,16</sup> with elastomer precursors or the in-situ reduction of metal  
2 nanostructures within the elastomer<sup>17–20</sup> have proven to be insufficient, as they result in either  
3 low electrical conductance or reduced mechanical stretchability or elasticity<sup>21</sup>. Alternatively,  
4 intrinsically stretchable organic conductors<sup>22,23</sup> or extrinsically configured structures, such as  
5 wrinkled/buckled<sup>14,24–26</sup> and kirigami structures<sup>27,28</sup>, could solve such performance issues.  
6 However, true metal-elastomer nanophases are still expected to be the far superior option,  
7 especially for usage in high-profit bioelectronic applications which require high-fidelity, long-  
8 term stable operation<sup>29</sup> in demanding microcosms within the human body<sup>30</sup>. This is because  
9 tailored metal-elastomer nanophases should excel in electrical performance, mechanical  
10 durability, and environmental resilience, where each characteristic is inherited from the  
11 respective metal and elastomer components. Nanoscale blending forms large interfaces that  
12 enhance the adhesion strength between metal and polymer<sup>31–33</sup>, as well as ‘softened’ metal  
13 nanoparticles and nanostructures result from high surface excess elasticity<sup>34</sup>. Additionally,  
14 highly percolated, and adaptable electrical conduction paths<sup>35,36</sup> open up untapped possibilities.

15 Noble metal deposition on elastomer templates has previously been utilized for stretchable  
16 conductors<sup>37–39</sup>. A particularly well-known approach is the thermal evaporation of gold (Au) on  
17 styrene-ethylene-butylene-styrene (SEBS) thermoplastic elastomers. During deposition, Au  
18 nanoparticles are interpenetrated into the SEBS elastomer and a metal-elastomer biphasic layer  
19 is formed, which enables a stretchable metal conductor<sup>37,38</sup>. However, the planar Au layer is  
20 easily cracked under micro- or nanoscale strain, leading to a rather narrow range of mechanical  
21 utilization. In addition, thermoplastic elastomers are vulnerable to heat and organic solvents,  
22 which limits their applications in environmentally challenging situations.

23 Even when nanoblending between immiscible materials is thermodynamically not  
24 preferred, kinetics can offer a way to overcome the limits imposed by the physical and chemical  
25 properties of materials. In this study, we introduce a kinetically controlled method for forming

1 a well-blended, metal-elastomer nanophase that is energetically unfavorable (**Figure 1**). This  
2 was accomplished by extensively exploring the utilization of the thermal evaporation method  
3 for polymeric substrates. While evaporation has been thoroughly investigated for thin film  
4 deposition in the past<sup>40</sup>, herein we revisited this technique from a kinetic point of view to mix  
5 metal atoms with elastomeric chains.

6 Vaporized metal atoms are free-form precursors that can be molded into different shapes,  
7 from nanoparticles and nanofilms to complex three-dimensional (3D) nanophases. A dramatic  
8 variety of structures and phases could emerge when metal atoms are deposited on elastomeric  
9 substrates, which can exist in different states ranging from liquid (uncrosslinked) mixtures to  
10 solid (fully crosslinked) slabs, depending on their degree of crosslinking. Even seemingly  
11 identical solid slabs could have different crosslinking networks and their molecular dynamics  
12 could vary drastically as a function of the amount of excess mobile molecules<sup>41–43</sup>. To  
13 investigate these phenomena and utilize them for nanoblending, we vaporized Au atoms on  
14 polydimethylsiloxane (PDMS) substrates with varying deposition thickness and base to  
15 crosslinker weight ratio,  $\phi$ , which is closely related to the migration flux of excessive  
16 crosslinkers.

17 These combinatorial methods reveal that the morphology of the resulting nanostructures  
18 can indeed be controlled, ranging from nanoparticulate, thin film, to complex 3D nanophases,  
19 as observed by optical and transmission electron microscopes (OM and TEM) (**Fig. 1b** and  
20 **Extended Data Figure 1**). This structural variety is also evident from the plasmonic color  
21 changes due to Au nanostructures (**Fig. 1c**). What first catches the eye from the images is the  
22 distinct formation of nanoparticulate phases, where nanoparticles are embedded in PDMS  
23 substrates, especially when  $\phi$  is less than 3. This trend showed up almost regardless of the  
24 deposition thickness. Note that the deposition thickness,  $d$  (nm), mentioned here indicates the  
25 thickness measured by the quartz crystal microbalance within the deposition chamber, which

1 can be considered as the product of process time,  $t_{process}$  (s), multiplied by the deposition rate  
2 ( $\text{\AA}/\text{s}$ ). This parameter was used to control the total amount of Au atoms deposited and compare  
3 the samples with each other. On the contrary, when  $\varphi$  is larger than 10, a thin metal film is  
4 formed, consistent with previous reports that utilize standard PDMS substrates for thin film  
5 transfer methods<sup>44-46</sup>. For intermediate values of  $\varphi$  ( $3 < \varphi < 10$ ), we observe 3D nanostructure  
6 phases that show structural variations ranging from elongated nanoparticles and needles to  
7 networked reticular complexes, as well as metal densification into PDMS as  $\varphi$  increases  
8 **(Extended Data Figure 1)**.

9        These Au-PDMS nanophases spontaneously form on the exposed surface of PDMS within  
10 the vacuum chamber, facilitated by the migration of excessive crosslinkers from the bulk  
11 material toward the surface. Inherently then, we should expect the thickness of the PDMS  
12 sample to also play a role in the nanophase formation process, since it governs the total volume  
13 capacity of excessive crosslinkers (see **Extended Data Figures 2 and 3**). Modulating the  
14 thickness of the PDMS membrane resulted in slight variations in the formation conditions for  
15 each nanophase; nevertheless, consistent trends emerged, indicating that increased PDMS  
16 thickness led to a higher occurrence of metal encapsulation due to higher migration flux. To  
17 gain more insight into the internal structures of these nanophases through the flow of electrons,  
18 we measured the electrical conductivity ( $\sigma$ ) for all conditions using a four-point probe method.  
19 Based on these measurements, we generated a simplified map (**Extended Data Figure 4**) that  
20 not only distinguishes between particle, reticular, and thin film phases but also enables  
21 estimation of the characteristic lengths within the reticular films, as they exhibit higher values  
22 when the Au-PDMS nanophases are more interconnected<sup>47</sup>.

23        The incorporation of metals into elastomers in kinetically mixed nanophases introduces  
24 inherent stress due to the moduli mismatch between the two constituents. Immediately after  
25 formation, the Au-PDMS nanophases can be considered to be in a state of mechanical

1 metastability, as they exhibit structural evolution over a relatively extended period of time  
2 (approximately 6 hours) following Au deposition (**Figs. 1d, e, and Supplementary Video S1**).  
3 We term this evolution process "gyrification" to distinguish it from common  
4 wrinkling/buckling. While the term "gyrification" is commonly used to describe the process of  
5 forming characteristic folds in the cerebral cortex (**Fig. 1h**), our investigation reveals a  
6 structural similarity, evident by white arrows in the correctional SEM image of **Fig. 1g** and the  
7 3D TEM tomography image of **Extended Data Figure 5**. Unlike conventional wrinkles or  
8 buckles, which primarily arise in thin metallic films on elastomeric substrates due to external  
9 forces like pre-stretched substrates, the gyrified 3D complexes in our study originate from  
10 internal stress within the blended nanophases.

11 The 3D nanophases presented here possess tangential stress gradients, granting them the  
12 necessary elasticity and malleability for nanoscale folding. In contrast, a conventional bilayer  
13 of metal film and PDMS can only experience buckling and lacks the ability to undergo  
14 gyrification due to the high energy cost associated with nanoscale creasing of the metal layer.  
15 The soft PDMS layer beneath the metal layer is insufficient to induce the necessary stress for  
16 folding in the stiffer metal layer. Although the bilayer structure can buckle to form mesoscopic  
17 wavy patterns, achieving folding at the nanoscale is extremely difficult because the stiffness of  
18 the metal layer increases exponentially as it deforms. **Gyrification can only be observed when**  
19 **the elastic moduli ratio of the two materials ( $\overline{E_{PDMS}/3E_{metal}}$ ) comprising a composite is high**  
20 **enough to form large amplitude but not too high to have less density.** A typical example is the  
21 human brain, which can be thought of as a rubber-rubber composite with similar elastic moduli.  
22 Detailed analytical mechanics with equations are provided in **Supplementary Note 1**, and  
23 complementary computational analysis will also be presented in **Figure 3** to support these  
24 observations.

1 To further investigate the formation kinetics of the Au-PDMS 3D nanophases, we  
2 manipulated the flux of Au atoms introduced to PDMS by varying the parameter  $\varphi$ . This  
3 allowed us to observe the interaction and competition between the migration flux of excessive  
4 crosslinkers and the deposition flux of Au atoms. Cross-sectional high-resolution TEM  
5 (HRTEM) images clearly illustrate that the nanophase morphology is governed by the relative  
6 flux difference (**Figs. 2a** and **2b**). Under fixed conditions of a deposition rate of 2.5 Å/s and a  
7 deposition thickness,  $d$ , of 100 nm, the nanophase morphology exhibits variations with  $\varphi$ ,  
8 transitioning from nanoparticles ( $\varphi = 2$ ), to reticular nanophases ( $\varphi = 3.5, 5$ ), and eventually to  
9 thin films ( $\varphi = 10$ ) (**Fig. 2a**). A similar trend is observed when the situation is reversed,  
10 maintaining a fixed  $\varphi$  of 3.5 and  $d$  of 100 nm but altering the deposition rates (**Fig. 2b**). **Notably,**  
11 **plasmonic color changes stemming from diverse Au nanostructures lend additional support to**  
12 **this observation (Fig. 2c).** As the shape of Au nanostructures shifted from nanospheres and  
13 nanorods to nanoneedles, the principal localized surface plasmonic resonance (LSPR) peaks  
14 exhibited a red shift, aligning with the electromagnetic simulation results (**Supplementary**  
15 **Note 2** and **Supplementary Fig. S2**). This reaffirms that the resulting nanophase is determined  
16 by the relative flux difference rather than the absolute value of individual fluxes.

17 These results suggest that in terms of growth kinetics, we can classify the nanophases into  
18 three distinct cases based on the competition between the excess crosslinker migration flux  
19 ( $J_{migration}$ ) and the Au deposition flux ( $J_{deposition}$ ) (**Fig. 2d, Supplementary Note 3**). The first  
20 case occurs when the migration flux significantly exceeds the deposition flux ( $J_{migration} \gg$   
21  $J_{deposition}$ ). Under these conditions, the Au nanoparticles become entirely enclosed by rapidly  
22 migrating excessive crosslinkers, preventing further metal coalescence and leading to the  
23 formation of particulate nanophases. This phenomenon is akin to sputtering Au atoms onto a  
24 liquid substrate using silicone oil, as previously reported<sup>48</sup>. In the second case, when the  
25 migration rate is comparable to the deposition rate ( $J_{migration} \approx J_{deposition}$ ), crosslinkers are unable

1 to completely cover the initially nucleated Au nanoparticles due to the limited migration time.  
2 Consequently, anisotropic growth of Au nanostructures is expected from the exposed areas as  
3 seed particles, which is schematically depicted in **Supplementary Fig. S3** and confirmed by  
4 TEM observations (**Supplementary Fig. S4**). The third case arises when the deposition rate  
5 greatly exceeds the migration rate ( $J_{migration} \ll J_{deposition}$ ), leading to the straightforward  
6 deposition of Au as a thin film. Under these conditions, the formation of a nanophase between  
7 Au and PDMS is suppressed, enabling the transfer of the metal film, referred to as an  
8 elastomeric stamp<sup>44-46</sup>.

9 To establish a correlation between the amounts of excessive crosslinkers and  $\varphi$ , we also  
10 conducted chemical characterizations using <sup>1</sup>H nuclear magnetic resonance (NMR).  
11 Specifically, we performed quantitative analysis on the intensity of peaks corresponding to  
12 silicon methyl ( $I_4$ ) and hydride groups ( $I_5$ ), which represent the base and crosslinkers,  
13 respectively (**Figs. 2e, f**). This approach allowed us to estimate the degree of crosslinking in the  
14 PDMS membrane by calculating the ratio of Si-H to Si-CH<sub>3</sub> ( $I_5/I_4$ ). The results revealed a clear  
15 negative correlation with  $\varphi$ , indicating an increase in material conjugation as  $\varphi$  increased (**Fig.**  
16 **2g**). Our findings align with the mechanism we proposed earlier and inferred from the HRTEM  
17 images; smaller  $\varphi$  values lead to the formation of nanoparticulate phases due to a higher number  
18 of excessive crosslinkers, which result in a higher migration flux. Larger  $\varphi$  values result in  
19 thinner nanophase thickness due to reduced migration, which is also consistent with the  
20 measured average value of thickness for samples with different  $\varphi$  values, as shown in **Figs. 2a**  
21 **and 2g**. Furthermore, the results of a direct contact printing experiment of the PDMS slab using  
22 Fourier-transform infrared (FTIR) spectroscopy provide additional support for these findings  
23 (**Supplementary Fig. S5**).

24 The spontaneous gyration of reticular nanophases, occurring within a few hours, stands  
25 out as one of the most distinctive aspects of our Au-PDMS composite material, setting it apart

1 from many other materials instantly formed from wrinkles/buckles. Notably, nanophases with  
2 different  $\varphi$  values exhibit significantly different structural evolution timescales and  
3 morphologies. For instance, the reticular nanophase ( $\varphi = 3.5$ ) undergoes gyrfication, leading  
4 to the formation of micrometer-scale deep, large furrows over a period of 6 hours (**Fig. 3a**). In  
5 contrast, the particulate nanophase ( $\varphi = 2$ ), initially characterized by fine and smaller (sub-  
6 micrometer) structures, develops furrows with micrometer-sized amplitudes within a shorter  
7 time frame of 2-3 hours (**Extended Data Figure 6**). The formation of such microstructures  
8 originates from the residual compressive stress within the nanophases. To identify the residual  
9 compressive stress accumulated at the interface between Au-PDMS nanophases and bulk  
10 PDMS, we conducted spatially resolved Raman spectroscopy on a freshly Au-deposited PDMS  
11 membrane with  $\varphi = 3.5$  (when the stress was not yet relaxed) and compared the spectra with  
12 those obtained from the same sample before deposition (**Fig. 3b**). Following Au deposition, the  
13 Raman peaks related to the Si–O–Si stretching of PDMS (centered at  $490.8 \text{ cm}^{-1}$ ) clearly  
14 showed a red-shift of  $\sim 5 \text{ cm}^{-1}$ , indicating the occurrence of significant spatial strain in the  
15 PDMS adjacent to the Au layer.

16 The Raman data are consistent with the results obtained from finite element method (FEM)  
17 simulations based on hyper-elastic material models (**Supplementary Note 4 and 5**).  
18 Specifically, we used a hyperelastic Mooney-Rivlin material with parameters derived from  
19 uniaxial tensile tests (see **Table S1** for the uniaxial tensile tests for the  $\varphi = 3.5$  PDMS). For the  
20 plain Au layer and the Au-PDMS layer (an elastic rectangular block of dimensions of  $24 \mu\text{m} \times$   
21  $24 \mu\text{m} \times 20 \mu\text{m}$  in  $x$ -,  $y$ - and  $z$ -direction), we used two geometrically exact Cosserat shells as  
22 described in the literature<sup>49</sup>. To model the swelling ratio, we attached a swollen plain Au layer  
23 and a swollen Au-PDMS layer to a stretched-out plain PDMS layer. After releasing the stretch  
24 on the plain PDMS layer, a 3D complex formed due to the stress mismatch. For all simulations,  
25 we chose the same maximum penetration depth of Au atoms as in the HRTEM images (**Figure**

1 **2a)**. There was almost no dependence on the deposition thickness in the case of  $\phi = 3.5$ , which  
2 corresponds to our experiments.

3 In our computational analysis, we explored the surface morphology using three key  
4 parameters: Young's modulus ( $E_Y$ ), the swelling ratio of the Au-PDMS nanophase layer ( $Q$ ),  
5 and the thickness of the top plain Au layer ( $t_{Au}$ ). Among the various experimental conditions,  
6 in particular we focused on the effect of deposition thickness on the swelling and releasing  
7 behavior of gyrified structures. In our simulations, we assumed that that with an increase in the  
8 process time,  $t_{process}$ , at a fixed deposition rate, both the swelling ratio of the Au-PDMS  
9 nanophase layer,  $Q$ , and Young's modulus,  $E_Y$ , also increase (**Fig. 3c**). The calculated surface  
10 morphology after stress release closely matched the experimental data in many aspects,  
11 including the shape, feature size, and general trend with increasing  $t_{process}$ . Notably, the  
12 transition from hexagonally arranged islands to a labyrinth pattern was confirmed when  $t_{Au}$  is  
13 80nm,  $Q$  is 1.3, and  $E_Y$  is 10 GPa, aligning well with observations in the HRTEM images. These  
14 results support our hypothesis that the spontaneous evolution of the 3D surface complex is  
15 initially driven by the compressive stresses of an Au-PDMS nanophase accumulated by  
16 excessive crosslinkers. However, it is important to note that the complete replication of gyrified  
17 experimental results with deep folds in simulations was challenging using this simplified FEM  
18 model, even when scanning all possible computational parameters. This is mainly because  
19 gyrification cannot be solely induced by compressive stresses with fixed force; rather, it  
20 involves a complex dynamic process that includes chemical migrations and changes in volume  
21 and compressive force vector over time.

22 Based on real-time OM observations (**Supplementary Video S1**), together with HRTEM  
23 morphologies and FEM simulations, we conclude that the gyrification phenomenon is initially  
24 driven by accumulated compressive stress. However, it is further influenced by the subsequent  
25 self-swelling of uncross-linked, low-molecular-weight PDMS oligomers for a couple of hours.

1 Macroscale expansion due to the self-swelling of oligomers was observed and quantified by  
2 measuring the change in a patterned deposition area (**Supplementary Figures S7 and S8**). The  
3 different nanophases exhibited variations in expansion: the reticular nanophase displayed a  
4 roughly 10% change in measured area, while the particulate nanophase showed an areal change  
5 of approximately 3%. Another strong piece of evidence suggesting the self-swelling of PDMS  
6 oligomers can be found by etching out metal layers after gyration. If the nanostructures  
7 collapse after the etching process, it indicates that there were no crosslinked PDMS  
8 nanostructures but only Au nanostructures with excessive crosslinkers. However, if they  
9 maintain their gyration morphologies even after the etching process of Au, it indicates that the  
10 PDMS oligomers themselves migrated and crosslinked to form the nanophase structures. It was  
11 observed that the gyration PDMS structures were maintained even without the Au layer (**Fig.**  
12 **3d**), strongly suggesting the self-swelling of oligomers as well as their crosslinking into  
13 reticular nanophases during the gyration processes.

14 As mentioned earlier, the primary goal of forming a metal-elastomer nanophase is to  
15 achieve elastomer-like stretchability while maintaining metal-like electrical conductivity. We  
16 argue that our Au-PDMS nanophase materials demonstrate such characteristics. In a sample  
17 with optimized parameters (1.25 mm thick PDMS membrane,  $\phi = 3.5$ , Au deposition rate of  
18  $2.5 \text{ \AA/s}$ , and  $d$  of 100 nm), we observe a conductivity as high as  $1.4 \times 10^4 \text{ S/cm}$  (**Fig. 4**). This  
19 initial conductivity obtained by four-point probe measurements did not change upon the  
20 application of uniaxial strain up to 150% (**Fig. 4a** and **Fig. 4b**, left panels) or areal strain up to  
21 156% (**Fig. 4a** and **Fig. 4b**, right panels). No mechanical failures, such as cracks or  
22 delamination, were observed during the stretching tests, confirming its rubber-like elasticity.  
23 Moreover, the initial conductivity remained constant after 10,000 stretching–releasing cycles  
24 with uniaxial and areal strains in the same range (**Fig. 4b**). Additionally, it exhibits superior

1 long-term stability, as the electrical performance remained virtually constant for more than 8  
2 years of shelf life (**Supplementary Fig. S9**).

3 Depending on the application, electrodes can generally be classified into two types: active  
4 and passive. Active electrodes are used to directly inject or extract currents into/from a system,  
5 while passive electrodes serve to carry currents between different components or parts of a  
6 circuit. Among these, strain-invariant electrical properties are especially important for passive  
7 bus lines, ensuring a stable and reliable conductive path within and between circuit elements.  
8 To address this importance and cater to practical applications, we studied the relative resistance  
9 of our 3D Au-PDMS nanophase samples by employing two-terminal measurements with  
10 electrode widths ranging from 1 to 5 mm (**Fig. 4c**).

11 The standout feature of our Au-PDMS nanophase is its invariance to strain, greatly  
12 surpassing other state-of-the-art materials (**Supplementary Table S2 and S3, Supplementary**  
13 **Fig. S10**)<sup>12–14,22,23,50</sup>. The ‘ideal elastic conductor’ in **Fig. 4c** depicts a hypothetical sample with  
14 strain-invariant resistivity in two-terminal measurements, only portraying the geometric change  
15 in resistance that would come with stretching, including considerations regarding Poisson's  
16 ratio (**Supplementary Fig. S11**). Under this condition, the calculated resistance increases by  
17 2.5 times at 100% uniaxial strain (calculation details in **Supplementary Note 6**). Comparing  
18 this to the measured resistance changes of our Au-PDMS, we arrive at a compelling discovery:  
19 even up to 30% uniaxial strain, the resistance changes of our samples were significantly lower  
20 than those of an ideal elastic conductor. This intriguing behavior comes from the unfolding of  
21 the 3D gyrified complexes upon stretching, effectively compensating for the increased  
22 resistance due to dimensional changes.

23 The experimental and calculated resistance changes under areal strain showed the same  
24 tendency, where the 3D Au–PDMS nanophase samples exhibited a smaller resistance change

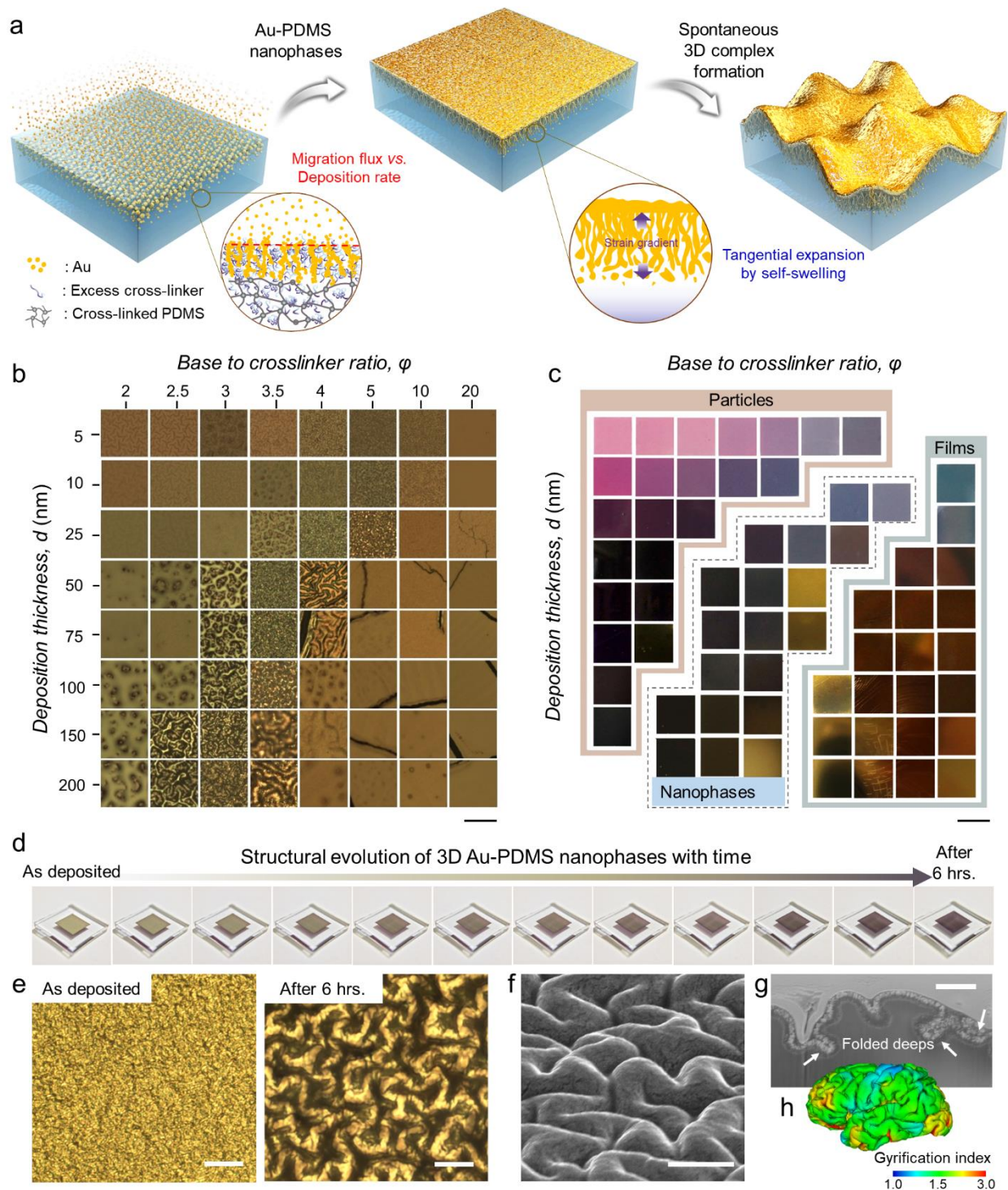
1 than an 'ideal elastic conductor' with up to 156% areal strain (**Fig. 4c**, lower, **Supplementary**  
2 **Fig. S12**). Note that areal strain, in this context, is distinctly different from biaxial strain, as  
3 areal strain involves 3D stretching using a sphere, while biaxial strain is limited to stretching  
4 within a 2D plane. To the best of our knowledge, we could not find any literature reporting  
5 conductive materials with such high areal strain sustainability (**Supplementary Table S3**). The  
6 unprecedented characteristics of our Au-PDMS nanophase material is primarily attributed to  
7 both the inherent stretchability of the reticular nanophases as well as the auxetic nature of the  
8 extrinsically gyrified 3D morphology (**Supplementary Fig. S13**). The combination of these  
9 intrinsic and extrinsic properties provides the high adhesivity and the structural, electrical  
10 elasticity required to prevent delamination and deterioration of electrical conductance in  
11 composite materials. Our view is further supported by the high gyrification index of 1.75  
12 calculated in our samples, which is defined as the ratio of the actual surface area to the  
13 projection area (**Fig. 4d**).

14 Following the remarkable electrical and mechanical properties of our gyrified reticular Au-  
15 PDMS nanophase samples, we showcase their multifaceted performance for applications in  
16 environmentally resilient soft electronics. Our samples display excellent stability against pH,  
17 chemical, and thermal exposure, as well as mechanical abrasion (**Fig. 5a** and **Supplementary**  
18 **Note 7**). After immersion in various polar and non-polar solvents (water, ethanol, acetone,  
19 chlorobenzene, and toluene) for 1 day, the conductivity of the nanophase samples slightly  
20 decreased, especially in organic solvents. This is possibly because of the deformed conduction  
21 network that comes from the swelling of the PDMS matrix itself. However, after the nanophases  
22 were dried, the conductivity almost fully recovered to within a 5% margin of error. Meanwhile,  
23 the conductivity was preserved under harsh pH conditions (pH 2–13), demonstrating this  
24 material's suitability for bioelectronics applications in the stomach (pH 1.3–3.5) as well as for  
25 use on skin wounds (pH 7.2–8.9). The conductivity of the gyrified Au–PDMS reticular

1 nanophases was also almost fully maintained during adhesive tape tests (ranging from 16 to 32  
2 N/cm) for 500 cycles. Even after an abrasion test using an eraser (**Supplementary Fig. S14** and  
3 **Supplementary Video S3**), the conductivity remained in the same order of magnitude (line of  
4 red symbols in **Fig. 5a**). In contrast to other thermoplastic elastomer-based stretchable  
5 electrodes, the gyri-fied Au–PDMS nanophases also showed excellent thermal stability up to  
6 250 °C for 2 h. This expands their potential use in interfacing with functional elements that  
7 require thermal annealing during fabrication and operation at elevated temperatures, such as  
8 thermoelectric and heater modules, or during hydrothermal sterilization processes (**Fig. 5a**,  
9 **Supplementary Video S4**, and **Supplementary Fig. S15**).

10 Furthermore, we also verified the reliability of the standard lithography process for the  
11 gyri-fied Au-PDMS nanophase (**Fig. 5b**). The chemical (organic solvents) and thermal (oven  
12 process for photoresist resin) durability of the Au–PDMS nanophase samples enabled  
13 microscale patterning down to a 20 μm feature size using conventional photolithography with  
14 complex circuit designs (**Supplementary Figs. S16 and 17**). The Au–PDMS nanophase  
15 samples were also found to be washable in a laundry machine. The initial conductivity and  
16 stretchability showed almost no change even after 20 cycles of 15 min. washing with detergent  
17 (**Supplementary Figs. S18, Supplementary Video S5**). These findings imply that this  
18 stretchable conducting membrane can be used to produce lithographically defined, functional  
19 devices intended for repeated use with reliable operation in the field of wearable electronics,  
20 including military and medical applications.

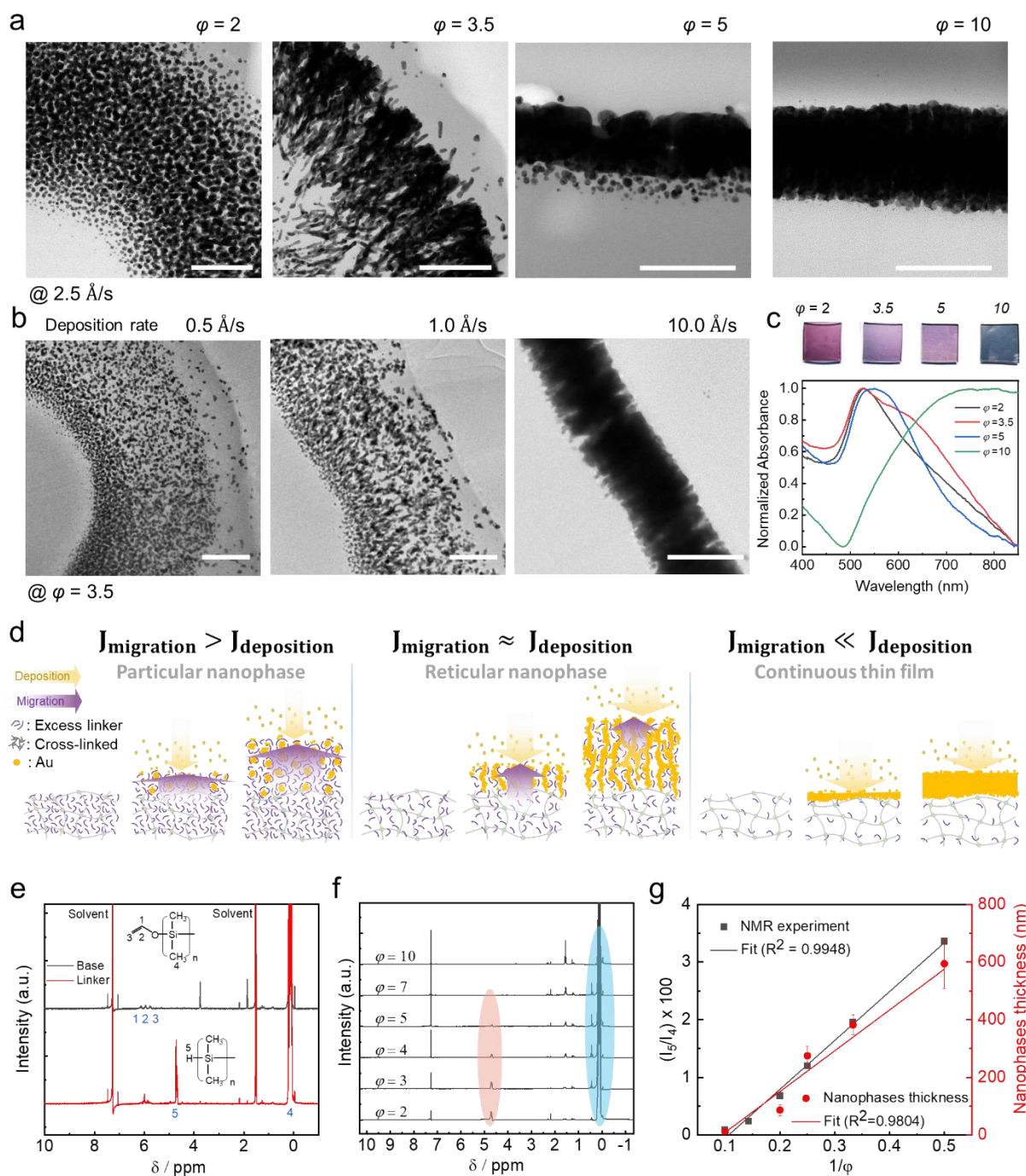
21 Our 3D complex of Au-PDMS nanophases holds considerable appeal as a stretchable  
22 conducting membrane for soft and bioelectronics applications and may find extensive use in  
23 various fields, including biomonitoring within the digestive tract, multimodal implantable  
24 devices like ocular prostheses, soft robotics employing mechanical strain-gated logic gates, and  
25 functional fabrics for space exploration.



1

2 **Figure. 1 | Spontaneously formed metal–elastomer nanophase and microscale 3D complex.**  
 3 **a**, Schematic illustration of the Au–PDMS nanophase self-forming via vaporized Au deposition  
 4 on a PDMS substrate. By varying the crosslinking ratio of PDMS and the deposition thickness  
 5 of metals, we controlled kinetics over three relevant dynamic processes: (1) migration of excess  
 6 crosslinker, (2) condensation of metal atoms into interlinked Au nanostructures, and (3) growth  
 7 of nanostructures and formation of the nanophase. Subsequently, spontaneous structural  
 8 evolution followed to form microscale 3D complexes owing to the stress inside. **b**, Surface  
 9 morphology change of Au–PDMS nanophases with various cross-linker to base ratios of base  
 10 PDMS polymer to curing agent in the elastomer substrate and deposition thickness of the metal.

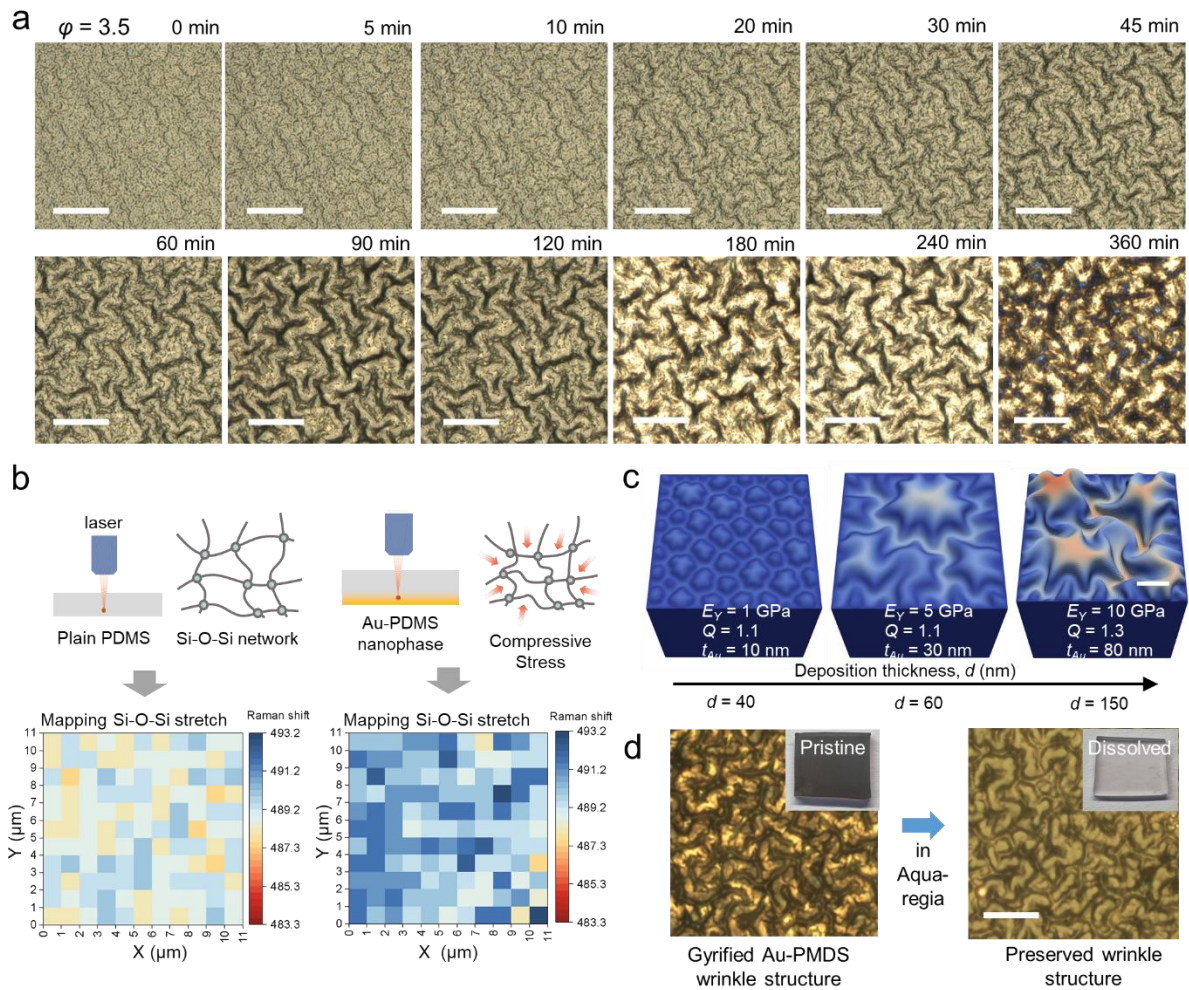
1 Scale bars denote 150  $\mu\text{m}$ . **c**, Photo images showing the corresponding colors of the samples  
2 for each condition. Three different of nanostructures were observed: “particles,” “3D  
3 nanophases,” and “continuous films.” Scale bars denote 1 cm. **d**, Photographs showing  
4 spontaneous structural evolution over a period of 6 h after Au deposition. The length of the  
5 PDMS and metal rectangles are 10 mm and 5 mm, respectively. The colors of the samples  
6 changed according to 3D complex evolution. **e**, Optical microscopy images of as-deposited and  
7 3D complex-formed (6 hrs.) samples. Scale bars in the optical microscopy images denote 150  
8  $\mu\text{m}$ . **f**, Tilted SEM image of gyrified wrinkles (scale bar is 5  $\mu\text{m}$ ). **g**, A cross-sectional SEM  
9 image of the gyrified structure. White arrows indicate folded deeps due to structural expansion  
10 (scale bar is 1  $\mu\text{m}$ ). **h**, An estimated local gyrification index (GI) of the human brain as an  
11 example akin to gyrified 3D structures. Adapted from ref.<sup>51</sup>  
12



1

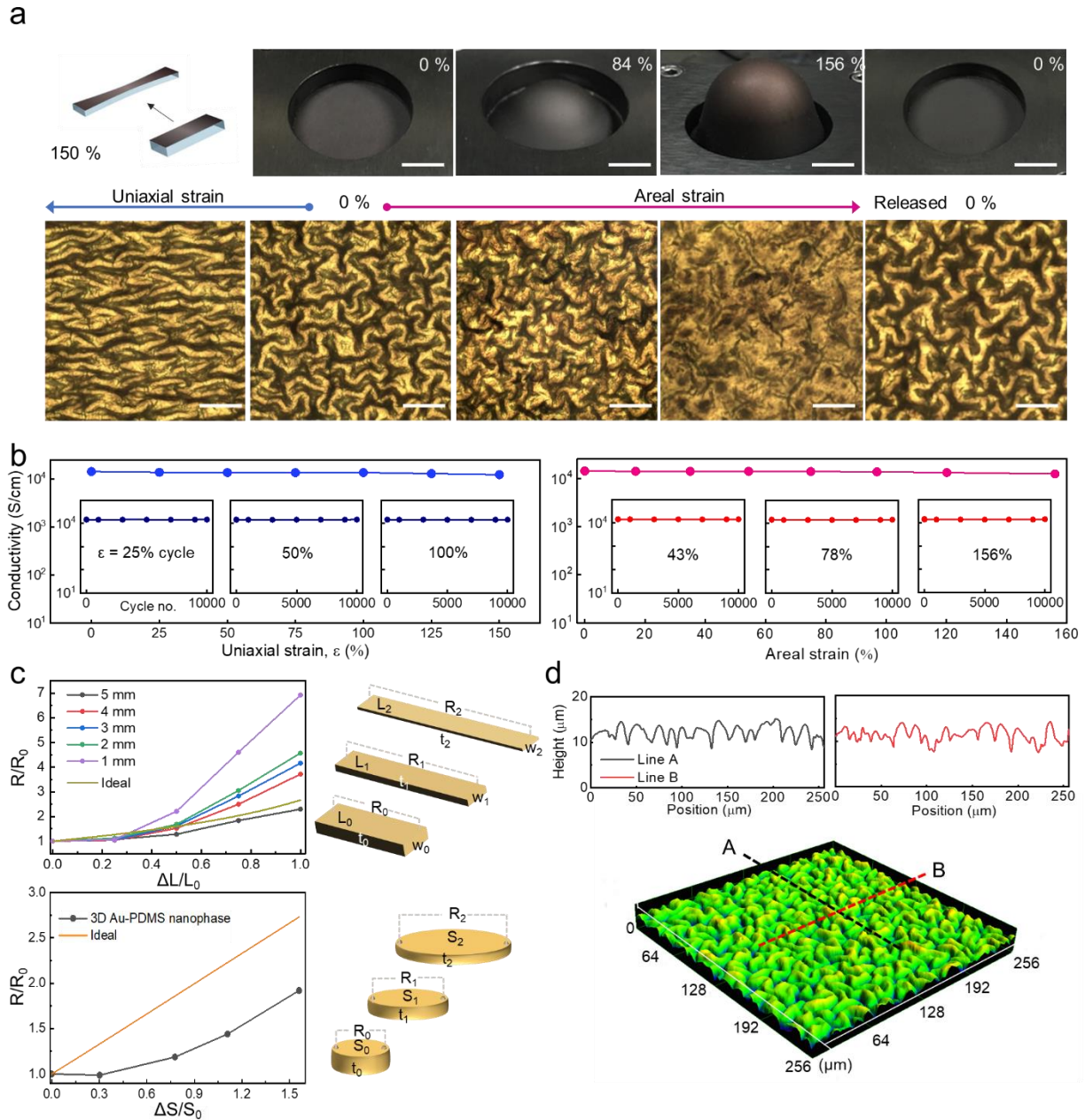
2 **Figure 2 | Growth Au-PDMS nanophases controlled by chemical kinetics.** Cross-sectional  
 3 HRTEM images of Au-PDMS membranes with **a**, various base to crosslinker weight ratio of  
 4 PDMS,  $\varphi = 2, 3.5, 5,$  and  $10$  at a deposition rate of  $2.5 \text{ \AA/s}$ , and with **b**, various deposition rates  
 5 of  $0.5, 1.0,$  and  $10.0 \text{ \AA/s}$  at  $\varphi = 3.5$ , displaying a variation in Au-PDMS membranes depending  
 6 on which kinetics is more dominant during the deposition (polymer migration versus rate of  
 7 metal deposition). Especially, the reticular nanophase formed at  $\varphi = 3.5$  at a deposition rate of  
 8  $2.5 \text{ \AA/s}$  is an internetworked and interpenetrated Au-PDMS nanophase. Scale bars denote  $200$   
 9 nm. **c**, Photo images of the samples (upper). Absorbance spectra of  $10 \text{ nm}$  Au-deposited samples  
 10 at  $2.5 \text{ \AA/s}$  on PDMS membranes with different crosslinker concentrations ( $\varphi = 2, 3.5, 5, 10$ )  
 11 (lower). **d**, A plausible nanophase formation mechanism. **e**,  $^1\text{H}$  NMR spectrum of neat PDMS  
 12 base polymer and PDMS curing agent. **f**,  $^1\text{H}$  NMR spectrum of  $\text{CDCl}_3$ , which was incubated  
 13 with PDMS at different mixing ratios of the two components. **g**, A negative correlation was  
 14 observed between the peak intensity ratio of Si-H to Si- $\text{CH}_3$  from the  $^1\text{H}$  NMR spectrum (**f**)

1 and  $\varphi$ , indicating a direct relationship between chain migration and the resulting nanophase  
2 morphology.  
3



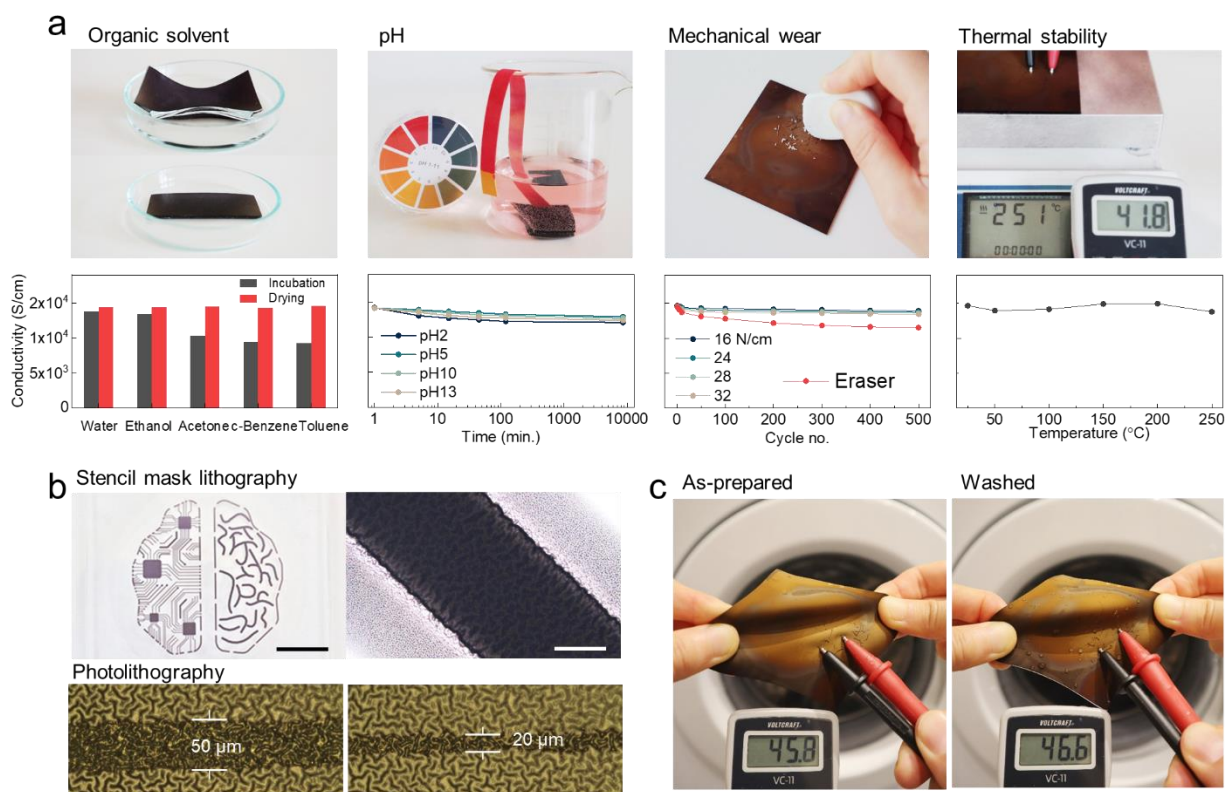
1  
2  
3  
4  
5  
6  
7  
8  
9  
10  
11  
12

**Figure 3 | Gyrification of Au-PDMS reticular nanophase.** **a**, Optical microscopy images showing the spontaneous gyrification of the Au-PDMS reticular nanophase after Au deposition over a period of 6 hrs. Scale bars in the photographs denote  $15 \mu\text{m}$ . **b**, Raman spectra of reference PDMS and Raman mapping image of plain PDMS Raman mapping image of as-Au-deposited substrate showing residual stress formed during the reticular growth of Au nanostructures inside the vacuum chamber. **c**, Finite element method (FEM) simulation of morphology features with three different mechanical parameters (upper), which match with the experimental 3D complex patterns with different Au deposition thicknesses. Scale bar denotes  $10 \mu\text{m}$ . **d**, Gyrified nanophase before and after dissolving Au was dissolved in aqua regia.



1  
2  
3  
4  
5  
6  
7  
8  
9  
10  
11  
12  
13  
14  
15  
16

**Figure 4 | Highly strain-invariant electrical conductivity achieved by the 3D Au-PDMS nanophase complex.** **a**, Optical microscopy (lower) and photo images (upper) showing stress dissipation by the gyrified 3D complex coupled with internal Au-PDMS nanophase upon applied strain both at uniaxial (leftwards) and areal (rightwards) strains. Strain-released images (0% at the outermost right side) shows the reversibility. Scale bars in the digital images denote 1 cm. Scale bar denotes in the optical microscopy images 150  $\mu\text{m}$ . **b**, Electrical conductivity of  $>10^4$  S/cm up to uniaxial 150% (left) and areal 156% (right) strain, along with cyclic stability over 10,000 cycles of each strain (insets). **c**, A strain-dependent relative resistance changes of the 3D complex of Au-PDMS nanophase samples with various electrode line widths (5, 4, 3, 2, and 1 mm). The experimental and simulated resistance changes are shown under the uniaxial (upper) and areal strain. **d**, Confocal microscopy image of the 3D complex of Au-PDMS nanophase samples showing that the high effective surface area contributed to the outstanding strain-invariant conductivity.



1  
2  
3 **Figure 5 | Multimodal stability and VR demonstration of the 3D complex of Au-PDMS**  
4 **nanophases. a**, Durability performance of the 3D complex of Au-PDMS nanophases as a  
5 function of various organic solvents, pH (pH 2–13), temperature (up to 250 °C), and severe  
6 abrasion by adhesive tape and eraser rubbing (from left to right). **b**, Patterning of the 3D  
7 complex of Au-PDMS nanophases using stencil mask lithography (upper, scale bar: 1 cm on  
8 the left and 50  $\mu\text{m}$  on the right) and conventional photolithography (lower), which can be  
9 realized for high-resolution patterning of stretchable electrodes. **c**, Washing test, displaying no  
10 degradation of electrical function under machine washing with detergent, as shown in movie  
11 S5.

12  
13  
14  
15  
16  
17 **REFERENCES**

- 18 1. Walheim, S., Schäffer, E., Mlynek, J. & Steiner, U. Nanophase-Separated Polymer Films  
19 as High-Performance Antireflection Coatings. *Science* **283**, 520–522 (1999).
- 20 2. Podsiadlo, P. *et al.* Ultrastrong and Stiff Layered Polymer Nanocomposites. *Science* **318**,  
21 80–83 (2007).
- 22 3. Faupel, F., Zaporozhchenko, V., Strunskus, T. & Elbahri, M. Metal-Polymer  
23 Nanocomposites for Functional Applications. *Adv Eng Mater* **12**, 1177–1190 (2010).

- 1 4. Haraguchi, K. Synthesis and properties of soft nanocomposite materials with novel  
2 organic/inorganic network structures. *Polymer Journal* vol. 43 223–241 Preprint at  
3 <https://doi.org/10.1038/pj.2010.141> (2011).
- 4 5. Beiner, M. & Huth, H. Nanophase separation and hindered glass transition in side-chain  
5 polymers. *Nature Materials* vol. 2 595–599 Preprint at <https://doi.org/10.1038/nmat966>  
6 (2003).
- 7 6. Vayyaprontavida Kaliyathan, A., Varghese, K., Nair, A. S. & Thomas, S. Rubber–rubber  
8 blends: A critical review. *Progress in Rubber, Plastics and Recycling Technology* **36**,  
9 196–242 (2020).
- 10 7. Deore, B. *et al.* Direct printing of functional 3D objects using polymerization-induced  
11 phase separation. *Nat Commun* **12**, 55 (2021).
- 12 8. Yun, G. *et al.* Liquid metal-filled magnetorheological elastomer with positive  
13 piezoconductivity. *Nat Commun* **10**, (2019).
- 14 9. Hanisch, C., Kulkarni, A., Zaporozhchenko, V. & Faupel, F. Polymer-metal  
15 nanocomposites with 2-dimensional au nanoparticle arrays for sensoric applications. in  
16 *Journal of Physics: Conference Series* vol. 100 (Institute of Physics Publishing, 2008).
- 17 10. Takele, H. *et al.* Tuning of electrical and structural properties of metal-polymer  
18 nanocomposite films prepared by co-evaporation technique. *Appl Phys A Mater Sci*  
19 *Process* **92**, 345–350 (2008).
- 20 11. Kim, Y. *et al.* Stretchable nanoparticle conductors with self-organized conductive  
21 pathways. *Nature* **500**, 59–63 (2013).
- 22 12. Chun, K. Y. *et al.* Highly conductive, printable and stretchable composite films of carbon  
23 nanotubes and silver. *Nat Nanotechnol* **5**, 853–857 (2010).
- 24 13. Park, M. *et al.* Highly stretchable electric circuits from a composite material of silver  
25 nanoparticles and elastomeric fibres. *Nat Nanotechnol* **7**, 803–809 (2012).
- 26 14. Rogers, J. A., Someya, T. & Huang, Y. Materials and Mechanics for Stretchable  
27 Electronics. *Science* **327**, 1603–1607 (2010).
- 28 15. Lacour, S. P., Wagner, S., Huang, Z. & Suo, Z. Stretchable gold conductors on  
29 elastomeric substrates. *Appl Phys Lett* **82**, 2404–2406 (2003).
- 30 16. Lee, S. *et al.* A Metal-Like Conductive Elastomer with a Hierarchical Wrinkled Structure.  
31 *Advanced Materials* **32**, (2020).
- 32 17. Goyal, A. *et al.* In situ Synthesis of Metal Nanoparticle Embedded Free Standing  
33 Multifunctional PDMS Films. *Macromol Rapid Commun* **30**, 1116–1122 (2009).
- 34 18. Berry Jr, K. R., Russell, A. G., Blake, P. A. & Keith Roper, D. Gold nanoparticles  
35 reduced in situ and dispersed in polymer thin films: optical and thermal properties.  
36 *Nanotechnology* **23**, 375703 (2012).
- 37 19. Chan, E. P., Smith, E. J., Hayward, R. C. & Crosby, A. J. Surface Wrinkles for Smart  
38 Adhesion. *Advanced Materials* **20**, 711–716 (2008).

- 1 20. Gao, N., Zhang, X., Liao, S., Jia, H. & Wang, Y. Polymer Swelling Induced Conductive  
2 Wrinkles for an Ultrasensitive Pressure Sensor. *ACS Macro Lett* **5**, 823–827 (2016).
- 3 21. Kim, J., Oh, J., Park, Y., Kim, J. J. & Jeong, U. Soft Conductive Interfacing for  
4 Bioelectrical Uses: Adhesion Mechanisms and Structural Approaches. *Macromolecules*  
5 **56**, 4431–4446 (2023).
- 6 22. Oh, J. Y. *et al.* Intrinsically stretchable and healable semiconducting polymer for organic  
7 transistors. *Nature* **539**, 411–415 (2016).
- 8 23. Trung, T. Q. & Lee, N.-E. Recent Progress on Stretchable Electronic Devices with  
9 Intrinsically Stretchable Components. *Advanced Materials* **29**, 1603167 (2017).
- 10 24. Khang, D.-Y., Jiang, H., Huang, Y. & Rogers, J. A. A Stretchable Form of Single-Crystal  
11 Silicon for High-Performance Electronics on Rubber Substrates. *Science* **311**, 208–212  
12 (2006).
- 13 25. Oyewole, O. K. *et al.* Micro-wrinkling and delamination-induced buckling of stretchable  
14 electronic structures. *J Appl Phys* **117**, (2015).
- 15 26. Bowden, N., Brittain, S., Evans, A. G., Hutchinson, J. W. & Whitesides, G. M.  
16 Spontaneous formation of ordered structures in thin films of metals supported on an  
17 elastomeric polymer. *Nature* **393**, 146–149 (1998).
- 18 27. Xu, L., Shyu, T. C. & Kotov, N. A. Origami and Kirigami Nanocomposites. *ACS Nano*  
19 **11**, 7587–7599 (2017).
- 20 28. Shyu, T. C. *et al.* A kirigami approach to engineering elasticity in nanocomposites  
21 through patterned defects. *Nat Mater* **14**, 785–789 (2015).
- 22 29. Li, Y., Li, N., De Oliveira, N. & Wang, S. Implantable bioelectronics toward long-term  
23 stability and sustainability. *Matter* **4**, 1125–1141 (2021).
- 24 30. Bettinger, C. J. Materials Advances for Next-Generation Ingestible Electronic Medical  
25 Devices. *Trends Biotechnol* **33**, 575–585 (2015).
- 26 31. Xie, Y., Zhang, J. & Zhou, T. Large-area mechanical interlocking via nanopores: Ultra-  
27 high-strength direct bonding of polymer and metal materials. *Appl Surf Sci* **492**, 558–  
28 570 (2019).
- 29 32. Zhao, S., Kimura, F., Kadoya, S. & Kajihara, Y. Experimental analysis on mechanical  
30 interlocking of metal–polymer direct joining. *Precis Eng* **61**, 120–125 (2020).
- 31 33. Jun, G., Lee, J.-W., Shin, Y., Kim, K. & Hwang, W. Solvent-aided direct adhesion of a  
32 metal/polymer joint using micro/nano hierarchical structures. *J Mater Process Technol*  
33 **285**, 116744 (2020).
- 34 34. Elsner, B. A. M., Müller, S., Bargmann, S. & Weissmüller, J. Surface excess elasticity  
35 of gold: Ab initio coefficients and impact on the effective elastic response of nanowires.  
36 *Acta Mater* **124**, 468–477 (2017).
- 37 35. Vieira, L. de S. *et al.* A review concerning the main factors that interfere in the electrical  
38 percolation threshold content of polymeric antistatic packaging with carbon fillers as  
39 antistatic agent. *Nano Select* **3**, 248–260 (2022).

- 1 36. Wang, G., Wang, C., Zhang, F. & Yu, X. Electrical percolation of nanoparticle-polymer  
2 composites. *Comput Mater Sci* **150**, 102–106 (2018).
- 3 37. Jiang, Y. *et al.* A universal interface for plug-and-play assembly of stretchable devices.  
4 *Nature* **614**, 456–462 (2023).
- 5 38. Lee, Y. *et al.* Standalone real-time health monitoring patch based on a stretchable organic  
6 optoelectronic system. *Sci Adv* **7**, (2021).
- 7 39. Kim, M. H. *et al.* Mechanically robust stretchable semiconductor metallization for skin-  
8 inspired organic transistors. *Sci Adv* **8**, (2022).
- 9 40. Minton Ohring. *Materials Science of Thin Films*. (Academic Press, 2002).  
10 doi:10.1016/B978-0-12-524975-1.X5000-9.
- 11 41. Tsujioka, T. Selective Metal-vapor Deposition on Organic Surfaces. *The Chemical*  
12 *Record* **16**, 231–248 (2016).
- 13 42. Tsujioka, T. & Matsumoto, S. Nucleation, absorption, or desorption of metal-vapor  
14 atoms on amorphous photochromic diarylethene films having a low glass transition  
15 temperature. *J Mater Chem C Mater* **6**, 9786–9793 (2018).
- 16 43. Nagaraja, S. M., Mujtaba, A. & Beiner, M. Quantification of different contributions to  
17 dissipation in elastomer nanoparticle composites. *Polymer* **111**, 48–52 (2017).
- 18 44. Lee, T. Il *et al.* Electrical contact tunable direct printing route for a ZnO nanowire  
19 Schottky diode. *Nano Lett* **10**, 3517–3523 (2010).
- 20 45. Lee, T. Il *et al.* Electrical contact tunable direct printing route for a ZnO nanowire  
21 Schottky diode. *Nano Lett* **10**, 3517–3523 (2010).
- 22 46. Meitl, M. A. *et al.* Transfer printing by kinetic control of adhesion to an elastomeric  
23 stamp. *Nat Mater* **5**, 33–38 (2006).
- 24 47. Choi, W. J. *et al.* High-performance carbon nanotube network transistors fabricated  
25 using a hole punching technique. *J. Mater. Chem. C* **1**, 4087–4093 (2013).
- 26 48. Wender, H., Migowski, P., Feil, A. F., Teixeira, S. R. & Dupont, J. Sputtering deposition  
27 of nanoparticles onto liquid substrates: Recent advances and future trends. *Coord Chem*  
28 *Rev* **257**, 2468–2483 (2013).
- 29 49. Bîrsan, M., Ghiba, I.-D., Martin, R. J. & Neff, P. Refined dimensional reduction for  
30 isotropic elastic Cosserat shells with initial curvature. *Mathematics and Mechanics of*  
31 *Solids* **24**, 4000–4019 (2019).
- 32 50. Dai, Y., Hu, H., Wang, M., Xu, J. & Wang, S. Stretchable transistors and functional  
33 circuits for human-integrated electronics. *Nature Electronics* vol. 4 17–29 Preprint at  
34 <https://doi.org/10.1038/s41928-020-00513-5> (2021).
- 35 51. Mietchen, D. & Gaser, C. Computational morphometry for detecting changes in brain  
36 structure due to development, aging, learning, disease and evolution. *Front Neuroinform*  
37 **3**, (2009).

- 1 52. Palchesko, R. N., Zhang, L., Sun, Y. & Feinberg, A. W. Development of  
2 Polydimethylsiloxane Substrates with Tunable Elastic Modulus to Study Cell  
3 Mechanobiology in Muscle and Nerve. *PLoS One* **7**, e51499 (2012).
- 4 53. Ramli, M. R., Othman, M. B. H., Arifin, A. & Ahmad, Z. Cross-link network of  
5 polydimethylsiloxane via addition and condensation (RTV) mechanisms. Part I:  
6 Synthesis and thermal properties. *Polym Degrad Stab* **96**, 2064–2070 (2011).
- 7 54. Kim, J.-H., Hwang, H.-S., Hahm, S.-W. & Khang, D.-Y. Hydrophobically Recovered  
8 and Contact Printed Siloxane Oligomers for General-Purpose Surface Patterning.  
9 *Langmuir* **26**, 13015–13019 (2010).

10

11

## 12 **Methods**

### 13 Kinetically Controlled Metal–Elastomer Nanophases

14 For the preparation of PDMS membranes, a mixture of two components, pre-base PDMS  
15 and linker PDMS (Sylgard 184, Dow Corning), was blended with varying ratios ( $\varphi = 2 - 20$ ).  
16 The mixture was subsequently thermally cured at 80°C for 4 hours. The PDMS membranes  
17 were affixed onto sample holders within a physical vapor deposition chamber manufactured by  
18 iNFOVION. To prevent any potential evaporation of small molecules within the PDMS slab,  
19 we maintained a consistent vacuum pressure for all samples. Gold (Au) was deposited using  
20 thermal evaporation at room temperature, with a constant base pressure of  $1.0 \times 10^{-6}$  Torr. The  
21 in-situ deposition rate and amount were monitored using a quartz crystal microbalance. The  
22 deposition rate of Au was maintained at 2.5 Å/sec for all samples, except for samples with  
23 varying deposition rates (ranging from 10 Å/sec to 0.5 Å/sec). A pre-deposition step was  
24 conducted for 1 minute at a constant rate of 2.5 Å/sec, with the shutter closed. The main  
25 deposition phase commenced by opening the shutter and continued for 400 seconds, resulting  
26 in the formation of a nanophase that exhibited optimal stretchable electrode performance.  
27 Following deposition, the samples were promptly removed from the chamber and allowed to  
28 age for 6 hours in ambient air. Subsequent characterization and analysis were performed  
29 without any additional surface treatments.

30 According to the materials safety data sheets (MSDS) for the base PDMS, it includes 0.5  
31 wt% xylene, 0.2 wt% ethylbenzene, >60 wt% dimethylvinyl-terminated dimethyl siloxane, 30  
32 to 60 wt% dimethylvinylated and trimethylated silica, and 1 to 5 wt% tetra(trimethylsiloxy)  
33 silane. Meanwhile, the MSDS for the Sylgard 184 ‘Curing Agent’ indicates 0.19 wt% xylene,  
34 <0.1 wt% ethylbenzene, 55 to 75 wt% dimethyl, methylhydrogen siloxane, 15 to 35 wt%  
35 dimethylvinyl-terminated dimethyl siloxane, 10 to 30 wt% dimethylvinylated and trimethylated  
36 silica, and 1 to 5 wt% tetramethyl tetravinyl cyclotetrasiloxane<sup>52</sup>. Additionally, a siloxane  
37 complex containing a few wt% platinum may be present in the curing agent as a catalyst, which  
38 we believe plays the most important role in crosslinking. However, the exact concentrations are  
39 unknown. Given these conditions, we believe that most experimentalists would agree that core  
40 components of base and crosslinker, would include difunctional vinyl-terminated PDMS chain  
41 as the base, where crosslinking occurs via the SiH-containing, a low molecular weight  
42 trimethylsiloxy-terminated PDMS with platinum catalysts assisting the formation of a siloxane  
43 cross-linking network<sup>53</sup>.

44 The viscosity of the base and the mixture immediately after mixing with the curing agent  
45 is 5500 mPa.s and 4000 mPa.s, respectively. For reference, the molecular weight of Sylgard  
46 184 has been reported to be about Mn ~ 4500 and MW~19000 (PI=4.24) in literature<sup>54</sup>.

## Stretching performance, mechanical and optical characterization

To uniformly apply uniaxial and areal strain to the 3D complex of Au-PDMS nanophases samples, a custom-made 1-D and 2-D screw-based stretching apparatus was integrated with an optical microscope (BX-51P, Olympus), confocal microscope, and a four-point probe station (Loresta-GP MCP-T600, MITSUBISHI CHEMICAL) for electrical property measurements. The strain rate used for the strain-dependent conductivity measurements was set at 10% per second. Cyclic stretchability, tested up to 10,000 cycles, was assessed using a stretching machine (Flexible Materials Tester, Hansung Systems, Inc.). For viscoelasticity measurements, dynamic mechanical analysis (DMA) was conducted using a TA Instrument Q800 instrument with a gas cooling accessory and a fiber/film tension modulus. Young's modulus of both plain PDMS and the 3D complex of Au-PDMS nanophases samples was determined using a MultiXtens II HP instrument from Zwick, following the DIN 53504/S2/30 protocol. The gyration index was determined from the data acquired through laser scanning confocal microscopy (LSM, Olympus LEXT OLS4100 laser scanning digital microscope). UV-Visible spectra of the samples were obtained using V-770 UV-Visible/NIR spectrophotometer. Raman mapping was obtained from Raman spectra of the samples in 10  $\mu\text{m}$  x 10  $\mu\text{m}$  area (LabRam Aramis, Horiba Jovin Yvon).

## TEM characterization

For the cross-sectional TEM images, PDMS samples were prepared as lamellar thin slices using focused ion beam (FIB) techniques with the JIB-4601F instrument from JEOL and the Quanta 3D FEG instrument from FEI. Subsequent TEM analysis was performed using a JEM-ARM 200F microscope from JEOL. To generate the 3D TEM tomography image of the Au-PDMS nanophases in the 3D complex sample, a series of tilted TEM images (30 images in total) were acquired by rotating the sample holder from  $-21^\circ$  to  $66^\circ$ . This process was carried out at a magnification of 50,000 with an exposure time of 0.5 seconds using a CCD camera (Orius SC200D, Gatan) mounted on an Ultra Corrected Energy Filtering Transmission Electron Microscope (UC-EF-TEM) system (Libra 200 MC TEM, Carl Zeiss). The acquired images were then subjected to an image reconstruction process, specifically Filtered Back Projection (TEMography), to generate the final 3D image.

## NMR characterization

The modulation of non-covalently tethered PDMS molecules within the PDMS matrix can be achieved by adjusting the base to crosslinker ratio. To characterize the residual solvent within the PDMS matrix, a series of free-standing PDMS membranes were immersed in  $\text{CDCl}_3$  for  $^1\text{H}$  nuclear magnetic resonance (NMR) analysis, allowing us to track the presence of uncrosslinked PDMS over time. Freshly cured PDMS membranes, prepared with varying  $\phi$  values, were sectioned into 4 x 5 x 10  $\text{mm}^3$  pieces and placed in an air-tight vessel containing 1.2 mL of  $\text{CDCl}_3$  (Eurisotop) for overnight incubation. Due to higher adsorption of the solvent by PDMS membranes with lower  $\phi$ , an additional 0.8 mL of  $\text{CDCl}_3$  was added after 60 minutes. Subsequently, a portion of each sample's supernatant was collected for  $^1\text{H}$  NMR measurements (500.13 MHz) using an AVANCE III 500 Spectrometer (Bruker, Germany) at a temperature of 30  $^\circ\text{C}$ .

## Micropatterning for integrated circuit

Photolithography of the 3D complex of Au-PDMS nanophase samples was carried out standard photolithography procedure. Specifically, the sample was spin-coated with a positive photoresist (positive AZ 5214E<sup>®</sup>, MicroChemicals) and then subjected to a soft bake at 110 $^\circ\text{C}$  for 2 minutes. Subsequently, the sample was exposed to a 365-nm UV light source (KLS-100H-

1 LS-150P, DONGWOO Optron) using a patterned photomask. After exposure, the sample was  
2 immersed in a developer solution (AZ<sup>®</sup> 327, MicroChemicals) with vigorous shaking for 1  
3 minute. A post-bake step at 190°C for 10 minutes was performed to ensure complete curing of  
4 the residual photoresist. Selective etching of the nanophase was achieved by incubating it in  
5 aqua regia, a mixture of HCl and HNO<sub>3</sub> in a 9:1 volume ratio. Any remaining photoresist was  
6 removed using a universal photoresist stripper (AZ<sup>®</sup> 100, MicroChemicals) for lift-off. For  
7 stencil mask lithography, a metal stencil mask (0.1 mm thick stainless steel, Devora Electronics)  
8 was placed directly on a plain PDMS membrane ( $\phi = 3.5$ , thickness 0.65 mm) without a spacer.

### 9 Environmental Resilience Test

10 To assess chemical stability, the as-fabricated 3D complex of Au-PDMS nanophase  
11 samples were immersed in various solvents (water, ethanol, acetone, c-Benzene, and toluene)  
12 overnight, followed by conductivity measurements (marked as 'incubation' in the 'Organic  
13 solvent' section of Fig. 4a). Subsequently, the samples were deswelled at 60°C overnight, and  
14 the conductivity was measured again (marked as 'drying' in the 'Organic solvent' section of Fig.  
15 4a). For pH stability testing, solutions of HCl and KOH were used to create different pH  
16 conditions. The as-fabricated samples were then immersed in the respective pH solutions for  
17 varying durations (up to 10,000 minutes). In the tape adhesion test, a strong adhesive tape (3M)  
18 was repetitively attached and detached from the surface of the 3D complex of Au-PDMS  
19 nanophases for 500 cycles. The conductivity change was measured after each attachment cycle.  
20 In the eraser test, the surface of the as-fabricated 3D complex of Au-PDMS nanophases was  
21 repeatedly rubbed with a pencil eraser (TOMBOW<sup>®</sup>) for a specified number of cycles. The  
22 rubbing strength was determined by the specific contact area (2 cm x 2 cm) and the applied  
23 push force, which was approximately 0.245 kPa, a force sufficient to generate eraser dust. This  
24 procedure was recorded in Supplementary Fig. S12 and Supplementary Video S3. Thermal  
25 stability trials were performed by heating the samples on a hot plate (SMHS-3, DAIHAN). The  
26 conductivity of the samples was evaluated after annealing at various temperatures. For the  
27 laundry test, the 3D complex of Au-PDMS nanophases sample (without encapsulation) was  
28 subjected to washing both with and without detergent (Persil Gel Detergent, Germany) in a  
29 washing machine (WW70T4042EE/EG, Samsung) for 15 minutes at room temperature. This  
30 washing procedure was repeated 20 times for the cyclic washing test.

### 31 **Acknowledgments**

32 We gratefully acknowledge Anik Kumar Ghosh, Uta Reuter and Petr Formánek, all from IPF  
33 Dresden, for assistance of FEM simulation, FIB and TEM analysis, respectively. Authors thank  
34 Jeeho Park, Minji Cho and Hyemin Park for assistance with image work, and Jonas Schubert  
35 and Duwon Jeong for fruitful discussions. Authors thank the Korea Basic Science Institute  
36 (KBSI) for the technical support. This research was supported by a National Research  
37 Foundation of Korea (NRF) grant funded by the Korean government (2021R1C1C1009925,  
38 2020R1A6A1A03048004, and 2020M2D9A3094171). This research was also performed  
39 within project LaSensA under the M-ERA.NET scheme and was funded by the Saxon State  
40 Ministry for Science, Culture and Tourism (Germany) and co-financed with tax funds on the  
41 basis of the budget passed by the Saxon state parliament and funded by the Deutsche  
42 Forschungsgemeinschaft (DFG, German Research Foundation)- CRC-1415 - 417590517. S.C  
43 and A.F. acknowledges support from the German Science Foundation with SPP 2100, project  
44 number 404941515. German Research Foundation grant 600/20-1 640690U12AB123456  
45 (LJN). This work is financially supported in part by German Research foundation (DFG) grants  
46 MA 5144/13-1, MA 5144/28-1 and Helmholtz Association of German Research Centres in the  
47 frame of the Helmholtz Innovation Lab "FlexiSens". This work was performed under the  
48 auspices of the U.S. Department of Energy by Lawrence Livermore National Laboratory under

1 Contract DE-AC52-07NA27344. W.J.C. gratefully acknowledge the LLNL LDRD Program for  
2 funding support of this project under No.22-ERD-056.

3 **Author contributions**

4 Conceptualization: JYO, SC, WJC, TIL

5 Methodology: JYO, SC, QAB, LJN, AK, CHC, PM, YZ, SA, OP, TIL

6 Investigation: SC, JYO, WJC, DM, QAB, LJN, AK, CHC, PM, YZ, SA, OP, TIL

7 Visualization: SC, JYO, QAB, LJN, CHC, PM, YZ, SA, OP, TIL

8 Funding acquisition: JYO, DM, TIL

9 Project administration: JYO, DM, TIL

10 Supervision: JYO, DM, WJC, AF, OS, SA, TIL

11 Writing: JYO, SC, WJC, DM, QAB, YJC, TIL

12 **Competing interests**

13

14 Authors declare that they have no competing interests.

15 **Data availability**

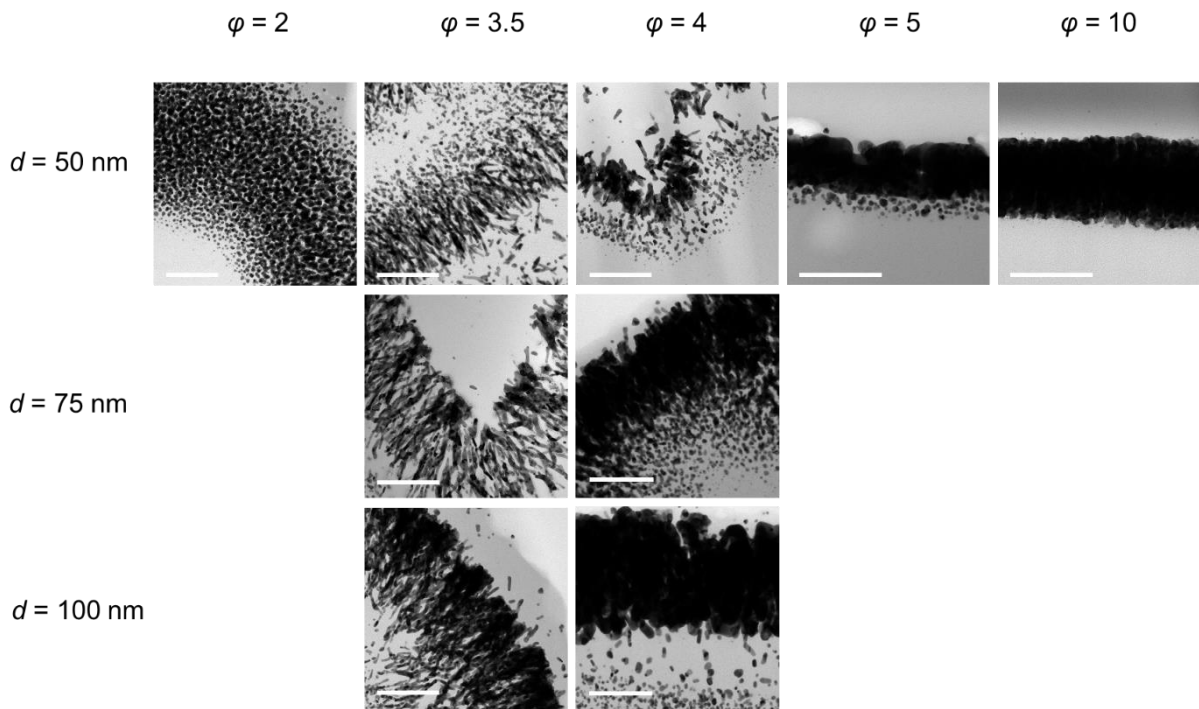
16 Data are available on request. Correspondence and requests for materials should be addressed  
17 to W.J.C., J.Y.O. and T.I.L.

18 **Supplementary information**

19 The online version contains supplementary material available at <https://doi.org/##.####>

1 **Extended data figures and tables**

2



3

4

5 **Extended Data Figure 1.** Cross-section HRTEM images of Au-PDMS nanophases with  
6 various  $\phi$  and deposition thickness of Au. Structural variety from particles, elongated  
7 nanoparticles, needles, to films was observed.

8

9

10

11

12

13

14

15

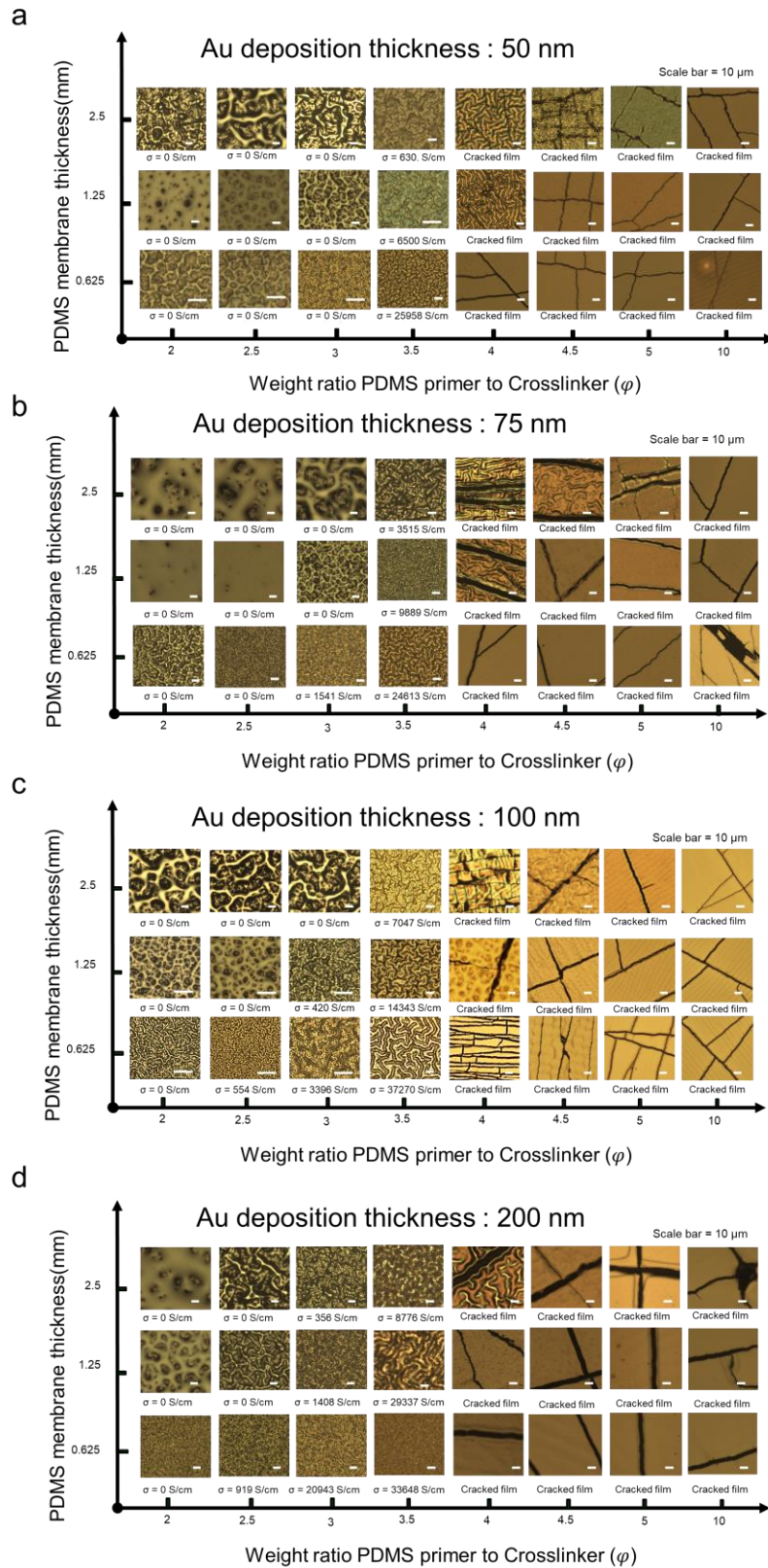
16

17

18

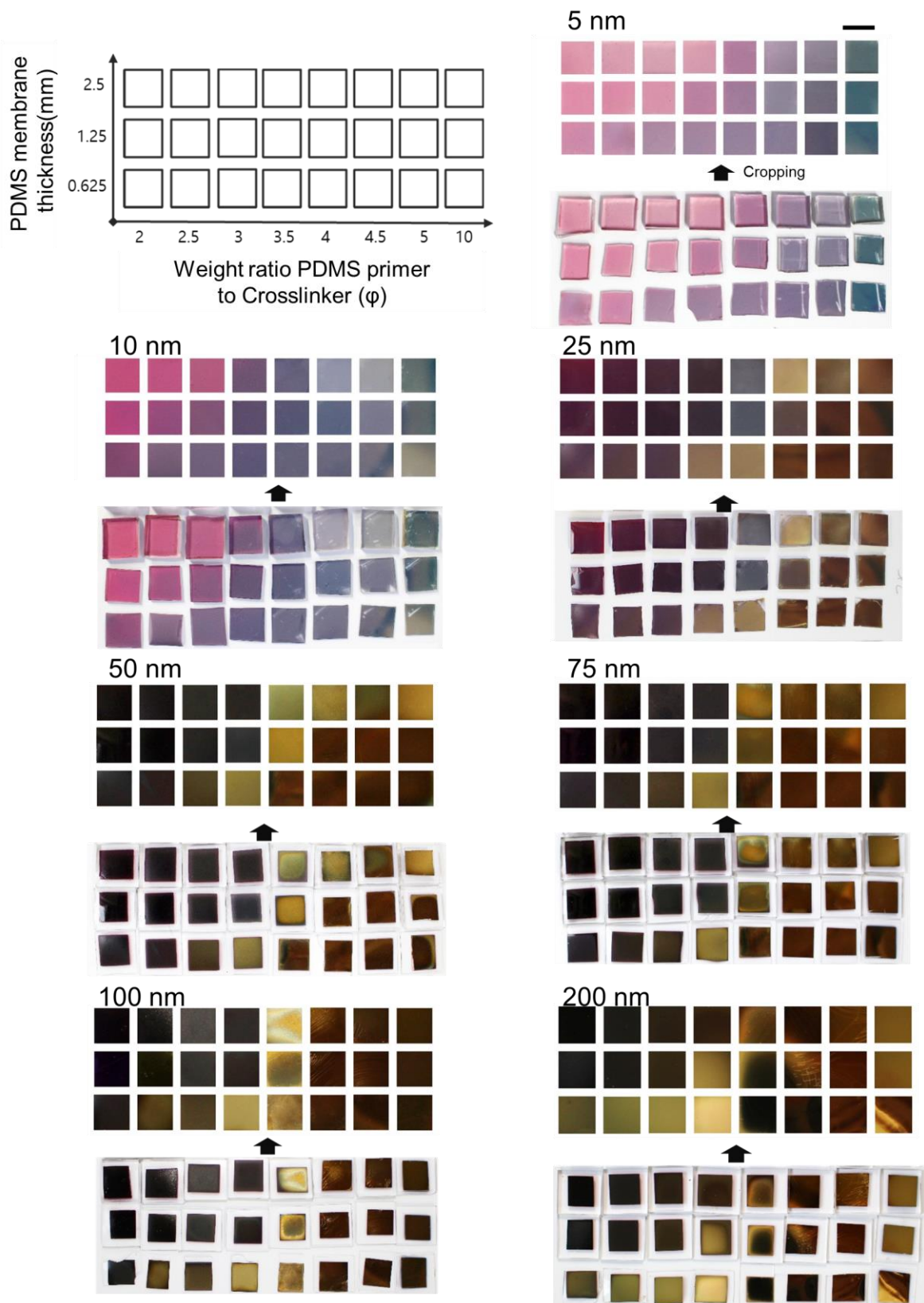
19

20



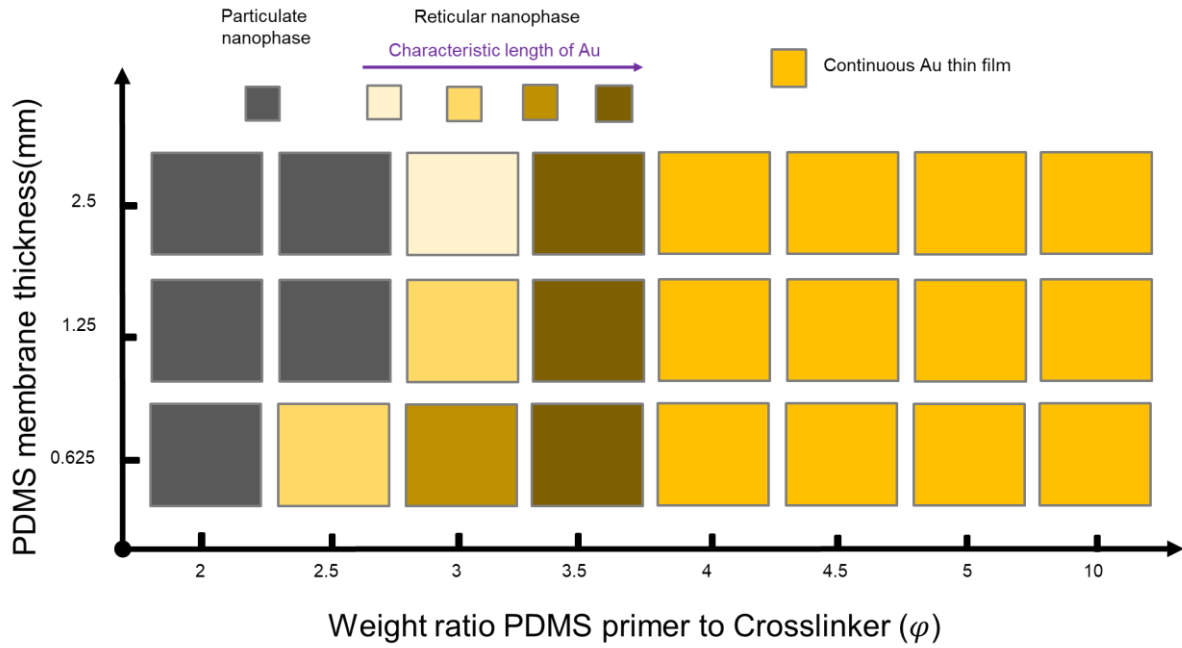
1

2 **Extended Data Figure 2.** Surface morphology changes and electrical conductivity of PDMS  
 3 membranes with deposited Au vary based on the mixing ratios ( $\phi$ ) of the base PDMS polymer  
 4 to the curing agent in the elastomer substrate, as well as different membrane thicknesses and  
 5 metal deposition thicknesses: (a) 50 nm, (b) 75 nm, (c) 100 nm, and (d) 200 nm. The  
 6 corresponding electrical conductivity, measured using the four-point probe method, also reveals  
 7 distinct features.



2

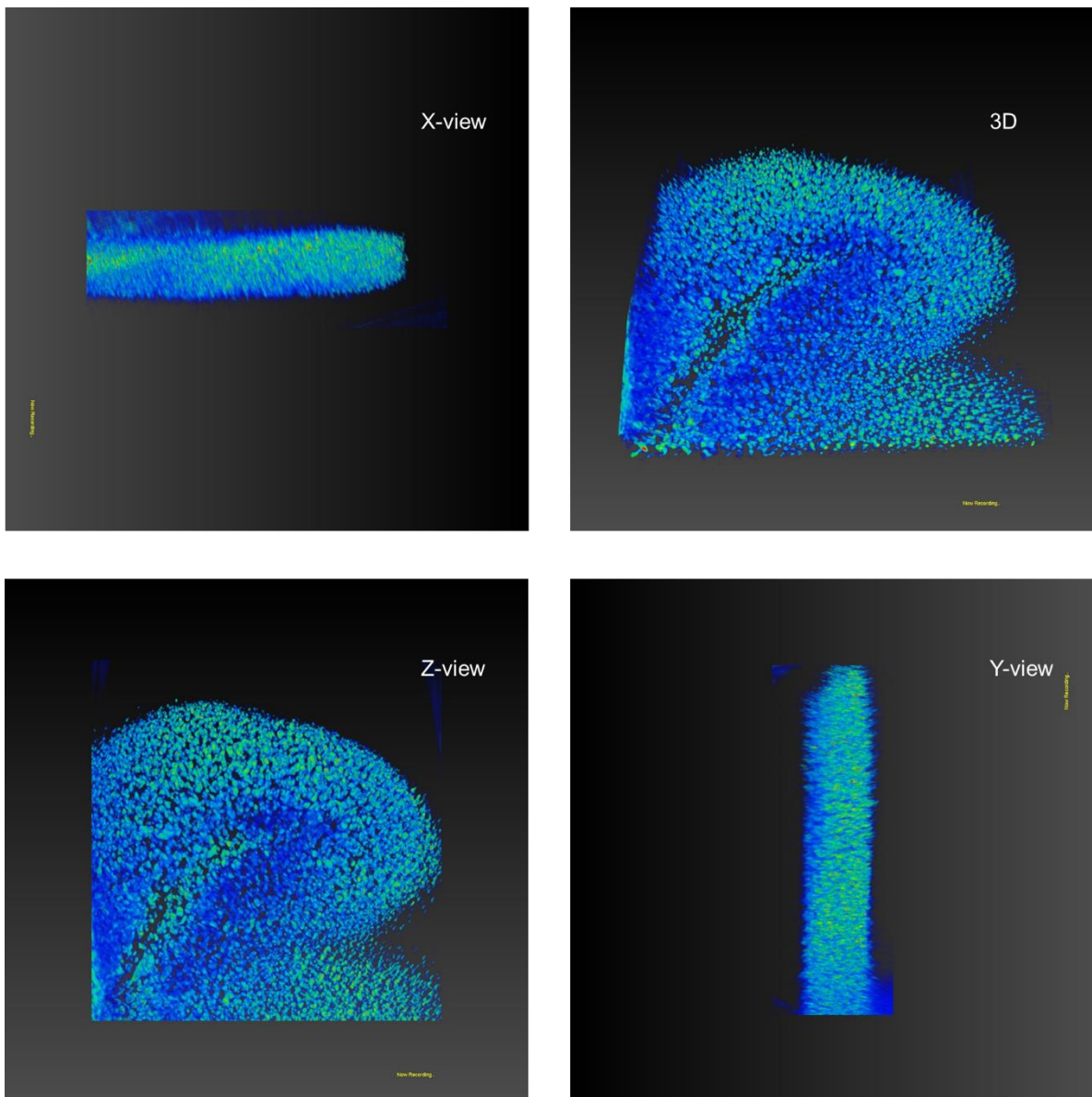
3 **Extended Data Figure 3. Variations in Au-PDMS membrane.** Photographs showing various  
 4 colors of Au-deposited PDMS samples with various mixing ratio ( $\phi$ ) of base PDMS polymer  
 5 to curing agent in the elastomer substrate, those membrane thickness, and deposition thickness  
 6 of the metal. Scale bars denote 1 cm.



1  
 2 **Extended Data Figure 4.** Classification table of Au-PDMS nanophases based on the process  
 3 variables; membrane thickness and  $\phi$  at 100 nm of deposition thickness. Conditions in which  
 4 electrical conductivity could not be measured were classified as having particulate nanophases,  
 5 and conditions in which electrical conductivity was measured were classified as reticular  
 6 nanophase.

7  
 8  
 9  
 10  
 11  
 12  
 13  
 14  
 15  
 16  
 17  
 18  
 19  
 20  
 21  
 22  
 23

1



2

3 **Extended Data Figure 5.** 3D TEM tomography images of Au 100 nm-thick deposited on the  
4 PDMS membrane ( $\varphi = 3.5$ ), showing the interconnected and interpenetrated gyri-like metal-  
5 elastomer nanophase. The brightness in the tomography images indicates 3D density of Au in  
6 the PDMS matrix. Scale bar = 300 nm.

7

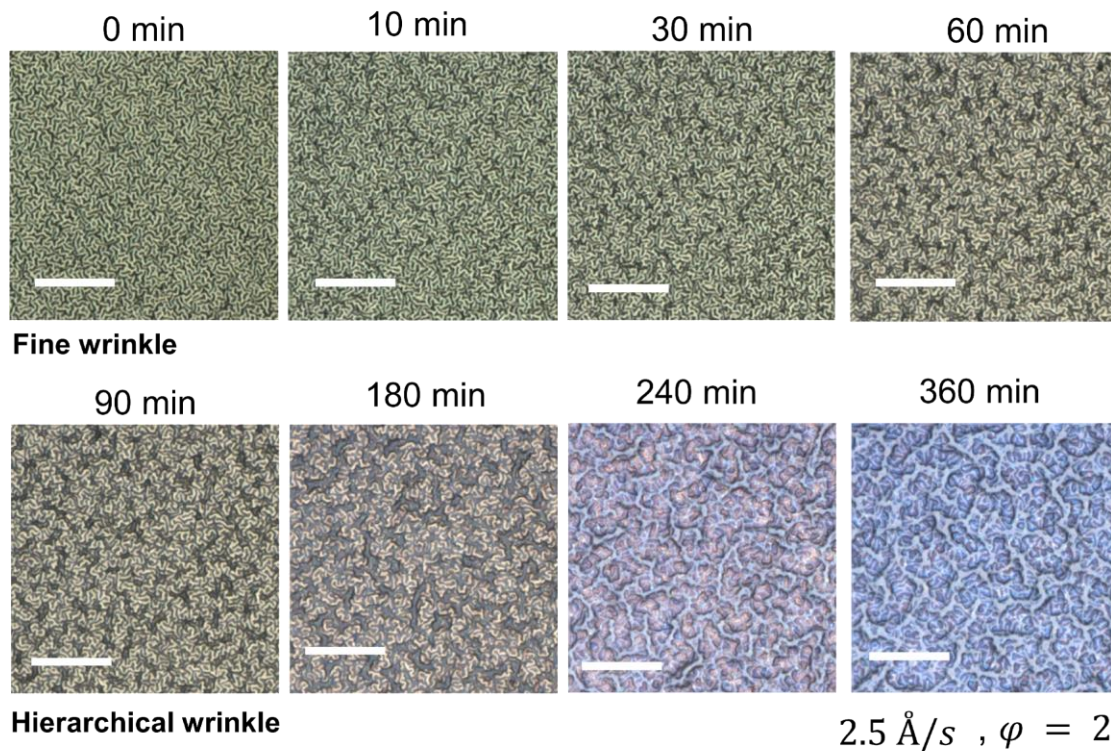
8

9

10

11

12



1  
 2 **Extended Data Figure 6.** LSM images of gyration of Au-PDMS nanophases at  $\varphi = 2.0$  and  
 3  $2.5 \text{ \AA/s}$ . The evolution of gyration at  $\varphi = 2.0$  occurs more rapidly compared to that at  $\varphi =$   
 4  $3.5$  resulting in distinct morphologies (as depicted in **Fig. 3a**). The scale bar corresponds to 10  
 5  $\mu\text{m}$ .